Journal of Luminescence 277 (2025) 120934

Contents lists available at ScienceDirect

Journal of Luminescence

journal homepage: www.elsevier.com/locate/jlumin

Full Length Article

On the photoluminescence of Pr(III) activated $Ca_2P_2O_7$ polymorphs

Tim Pier [*], Franziska Schröder, Jan Kappelhoff, Julia Hopster, Thomas Jüstel

FH Münster University of Applied Sciences, Dpt. Chemical Engineering, Stegerwaldstr. 39, D-48565, Steinfurt, Germany

ARTICLE INFO

Keywords:
Pyrophosphates
Luminescence
Praseodymium
Temperature dependent spectroscopy
UV-C phosphors

ABSTRACT

In this work the optical properties of two distinct, praseodymium activated, UV-C emitting pyrophosphate polymorphs are presented. The materials were obtained as single-phase samples using a facile solid state method with annealing at target phase-dependent temperatures. The activator concentration dependent luminescence quenching was investigated revealing significant differences between the $[Xe]4f^2 \rightarrow [Xe]4f^2$ and the $[Xe]4f^15d^1 \rightarrow [Xe]4f^2$ transitions. The highest emission intensities were observed at Pr^{3+} concentration of 0.5 and 2.0 % for the $[Xe]4f^2 \rightarrow [Xe]4f^2$ line and the $[Xe]4f^15d^1 \rightarrow [Xe]4f^2$ band emission, respectively. Furthermore, temperature dependent fluorescence spectroscopy and VUV spectroscopy were employed to investigate the thermal quenching behaviour as well as the excitation and emission properties in the deep UV range. Fitting of the temperature dependent emission integrals showed thermal quenching temperatures exceeding 700 K. It was revealed that the samples show two types of emission that can be traced back to the inter- and intraconfigurational transition of trivalent praseodymium. Praseodymium emission bands around 235 and 265 nm correspond to the various $[Xe]4f^15d^1 \rightarrow [Xe]4f^2$ interconfigurational transitions. Meanwhile, narrow emission lines throughout the visible and NIR range are caused by the $[Xe]4f^2 \rightarrow [Xe]4f^2$ intraconfigurational transitions of Pr^{3+}. Qualitative and quantitative comparisons between the emission properties of the two polymorphs revealed significant differences arising from the different coordination environments. α-$Ca_2P_2O_7$:Pr phosphors exhibited around 60 % of the emission intensities of the β-$Ca_2P_2O_7$ materials in the red spectral range while a reversed trend was observed for the UV emission caused by $[Xe]4f^15d^1 \rightarrow [Xe]4f^2$ transitions.

1. Introduction

The salts, esters, and polymers of orthophosphoric acid (H_3PO_4) are widely known as phosphates. They form a large group of inorganic compounds that are structurally defined by some type of $[PO_4]^{3-}$ anion differentiated from each other by the degree of polymerisation and condensation of these moieties [1–5]. Characterized by a combination of wide bands gaps, excellent photostability, and facile synthetic conditions, phosphates host structures have been the focus of a numerous studies exploring their use as luminescent materials. In addition they serve as model host structures for the general investigation of luminescent phenomena [6–9]. Foremost among these are orthophosphates, which have been extensively studied, even leading to the commercial application of $LaPO_4$:Ce,Tb, $LaPO_4$:Ce, and YPO_4:Ce in fluorescent lamps for illumination or tanning [10,11]. Among the phosphates, calcium phosphates form a subgroup containing oxide and hydroxide minerals, that have been investigated and utilized as biomaterials, catalysts, fertilizer, reflective pigments for fluorescent lamps, and agents for purifying heavy metal-contaminated water [12–15]. Due to their high biocompatibility, stemming from compositional and structural similarities to vertebrate bone material, calcium phosphates of the type $Ca_2P_2O_7$ have been considered and used as an additive in bone cements used for prosthetic implants and as an abrasive in toothpaste [16–18]. Further biomedical applications of calcium phosphates include the use of β-$Ca_2P_2O_7$ as a drug carrier, $Ca_3(PO_4)_2$ doped by Eu^{3+} and Gd^{3+} for bioimaging, and the creation of paramagnetic iron doped calcium phosphate nanocomposites for the hyperthermic treatment of cancer cells [19–21]. Cheap starting materials and facile synthetic conditions have made calcium pyrophosphates interesting as host structures for fluorescent materials. Especially the substitution of Ca^{2+} by isovalent activators such as Mn^{2+} and Eu^{2+} has been considered. *Hao* et al. suggested Eu^{2+} and Mn^{2+} co-doped α-$Ca_2P_2O_7$ as a phosphor for white light emitting LEDs [22,23]. The phase dependent optical properties of Mn^{2+} substituted $Ca_2P_2O_7$ polymorphs were investigated by *Griesiute* et al. [24]. Further photoluminescence studies include the doping by Eu^{2+} solely, which results in a broad band emitting blue phosphor, as well as

---

[*] Corresponding author.
E-mail address: timpier@fh-muenster.de (T. Pier).

https://doi.org/10.1016/j.jlumin.2024.120934
Received 4 July 2024; Received in revised form 2 October 2024; Accepted 3 October 2024

the doping by Eu^{3+}, Dy^{3+}, or Tb^{3+} [25–28].

Trivalent praseodymium is characteristically employed to take advantage of the combination of quantum mechanically allowed interconfigurational *[Xe]4f¹5d¹* → *[Xe]4f²* and forbidden intraconfigurational *[Xe]4f²* → *[Xe]4f²* transitions [29,30]. Consideration of the general energetic location of the *[Xe]4f¹5d¹* → *[Xe]4f²* transitions in the deep UV range, brands wide band gap materials such as phosphates interesting as host structures for praseodymium, to produce UV emitting phosphors. Fabrication of these deep UV-C emitting phosphors is of interest for many fields such as pathogen inhibition, water treatment, scintillation, and highly localized tumour treatment [31,32]. To best of our knowledge only one study covered praseodymium doped calcium pyrophosphates to this point. *Caiut* et al. compared several UVC emitting phosphates among them α-phase $Ca_2P_2O_7$ [33]. In the present work, we deliver to the best of our knowledge a new approach for the synthesis of single-phase α-$Ca_2P_2O_7$ materials. Additionally, we studied the emission properties in the UV and visible range of both polymorphs dependent on activator concentration and temperature. Differences in emission intensities and lifetime were explained by considering the crystal structure and highlighting the structure-property relationship of the Pr^{3+} activator and the pyrophosphate host structure.

2. Experimental section

2.1. Synthetic procedure

Two series of praseodymium doped pyrophosphates either belonging to the α-$Ca_2P_2O_7$ or the β-$Ca_2P_2O_7$ phase were successfully prepared employing a solid-state method. Stoichiometric amounts of $CaCO_3$ (Alfa Aesar, 99.5 %), $(NH_4)_2HPO_4$ (Merck KGaA, 99.0 %), P_2O_5 (VWR Chemical, 99.9 %), Na_2CO_3 (Merck KGaA, 99.9 %), and $Pr_2(C_2O_4)_3 \bullet 10H_2O$ (Alfa Aesar, 99.9 %) were used as starting materials. All reactants were transferred to an agate grinding container and ground for 30 min in a planetary ball mill. Afterwards, the powder mixtures were dried and transferred to corundum crucibles. These crucibles were placed in a chamber furnace and a reducing CO atmosphere was created using a larger crucible filled with activated charcoal. The formation of the desired phases was controlled by the annealing temperature, viz. 30 min at 1150 °C for β-$Ca_2P_2O_7$ and 30 min at 1250 °C for α-$Ca_2P_2O_7$. Additionally, a second crucible filled with P_2O_5 was placed adjacent to the educt mixture for the α-$Ca_2P_2O_7$ samples to create a "phosphate atmosphere". Following the heat treatment all samples were washed in deionized water for 2 h at 70 °C. After filtration the powders were dried overnight at 50 °C.

2.2. Material characterization

The formation of the desired phase and the phase purity was investigated and verified by powder X-ray diffractometry (PXRD). A powder x-ray diffractometer of the type *X'Pert Pro* produced by *Malvern Panalytical* was used for all diffraction experiments. The instrument was operated in a *Bragg-Brentano* geometry and equipped with a copper X-ray tube (Cu K_α – 0.154184 nm, 40 kV and 40 mA). All samples were measured between $2\theta = 10–80°$ with a step width of 0.017° and a scan speed of 0.084°/s. Depictions of the crystal structure were created using *VESTA 3* [34].

Phase pure powders were subjected to a thorough optical characterization using different, modified fluorescence spectrometers originally produced by *Edinburgh Instruments*. Diffuse reflectance spectra were recorded on a *FS920* spectrometer featuring a PTFE-coated *Ulbricht* sphere. A 450 W xenon arc lamp was used as an irradiation source. Two *TMS300* gratings (1800 grooves/mm) served as monochromators and a *Peltier* cooled (−20 °C) *R928* PMT-detector (*Hamamatsu*) as the detection unit. $BaSO_4$ (99.99 %, *Sigma Aldrich*) was used as the white reference standard. Samples were investigated in a range from 250 to 800 nm. Excitation and emission spectra were recorded on a *FLS920* fluorescence spectrometer outfitted with an ozone generating 450 W xenon discharge lamp. The recorded emission spectra were corrected by a correction file generated from a tungsten incandescent lamp by the *National Physical Laboratory* (NPL, UK). The spectrometer was additionally supplemented by a liquid nitrogen cooled cryostat (*MicrostatN2, Oxford Instruments*) as well as a temperature-controlled sample holder to investigate the temperature dependent excitation and emission behaviour between 77 and 500 K. The decay behaviour of the samples was investigated on the same spectrometer, in which the standard xenon lamp was replaced by a flash lamp of the type *μF920H* from *Edinburgh Instruments*. Afterwards, the recorded decay curves were fitted using mono- or multiexponential functions.

3. Results and discussion

3.1. Powder diffraction and crystal chemistry

Powder diffraction patterns of the two $Ca_2P_2O_7$ phases doped by Pr^{3+} are shown in Fig. 1. The synthesis resulted in single phase microcrystalline powders that are in good accordance with the presented reference patterns. Incremental substitution of Ca^{2+} by Pr^{3+} (and Na^+ as a means towards charge balance) resulted in no additional reflexes. Therefore, a successful incorporation of the praseodymium activator into the host structure is assumed. Several publications investigating α-$Ca_2P_2O_7$ materials reported on an impurity phase, mainly $Ca_3(PO_4)_2$ [24,35]. Formation of this secondary phase can be seen as a deviation from an ideal Ca/P ratio of 1:1 (in $Ca_2P_2O_7$) towards a Ca rich Ca/P ratio (in $Ca_3(PO_4)_2$), indicating the loss of phosphate moieties during the annealing process. This was indeed confirmed in several studies concerning the impact of different annealing conditions on the phase formation in the CaO/P_2O_5 phase diagram [36–38]. Specifically in a study by *Griesiute* et al., the evaporation of phosphate species was encouraged in a vacuum sintering process, leading to the complete transformation of $Ca_2P_2O_7$ to $Ca_3(PO_4)_2$ [39]. While the nature of the specific evaporated species is currently unknown, the process can be expressed stoichiometrically as follows.

$$3\ Ca_2P_2O_7 \rightarrow 2\ Ca_3(PO_4)_2 + P_2O_5\uparrow$$

In this study we were able to suppress the formation of $Ca_3(PO_4)_2$ by placing a separate crucible filled with P_2O_5 adjacent to the crucible containing the educt mixture. Both were then positioned inside a sealed crucible filled with activated carbon. Upon heating the P_2O_5 melts and evaporates, forming a saturated atmosphere effectively hindering the evaporation of phosphate species from the educt mixture. The PXRD pattern of this adjustment is shown in Fig. S4, where under the same annealing conditions $Ca_3(PO_4)_2$ is either formed or not, depending on the addition of P_2O_5.

For the calcium pyrophosphates three distinct crystallographic phases are known, named γ-$Ca_2P_2O_7$, β-$Ca_2P_2O_7$, and α-$Ca_2P_2O_7$. Structures of the α- and β-modifications have been known since the 1970s and were solved using single-crystal X-ray diffraction experiments. The formation of metastable polymorphs has to this day hindered the synthesis of γ-$Ca_2P_2O_7$ single crystals. Therefore, just recently has the structure of γ-$Ca_2P_2O_7$ been solved using X-ray powder diffraction and ^{31}P high-resolution solid-state NMR-spectroscopy [40]. The polymorph γ-$Ca_2P_2P_7$ was identified to crystallize in the triclinic space group *P*-1 (no. 2) and belonging to the $Cd_2P_2O_7$ structure type [41]. α-$Ca_2P_2O_7$ and β-$Ca_2P_2O_7$ crystallize in the space groups $P2_1/n$ (monoclinic, no. 14, Z = 4) and $P4_1$ (tetragonal, no. 76, Z = 8) respectively. Phase transition temperatures between the three phases are reported to be 750 °C (γ-$Ca_2P_2O_7$ → β-$Ca_2P_2O_7$) and 1170 °C (β-$Ca_2P_2O_7$ → α-$Ca_2P_2O_7$) [42]. Like all phosphates these materials are characterized by some form of tetragonally coordinated $[PO_4]$ moiety. In case of the di- or pyrophosphates two corner sharing phosphate tetrahedrons are connected along a P-O-P bond into $[P_2O_7]$ dimers. In detail, the tetragonal β-structure

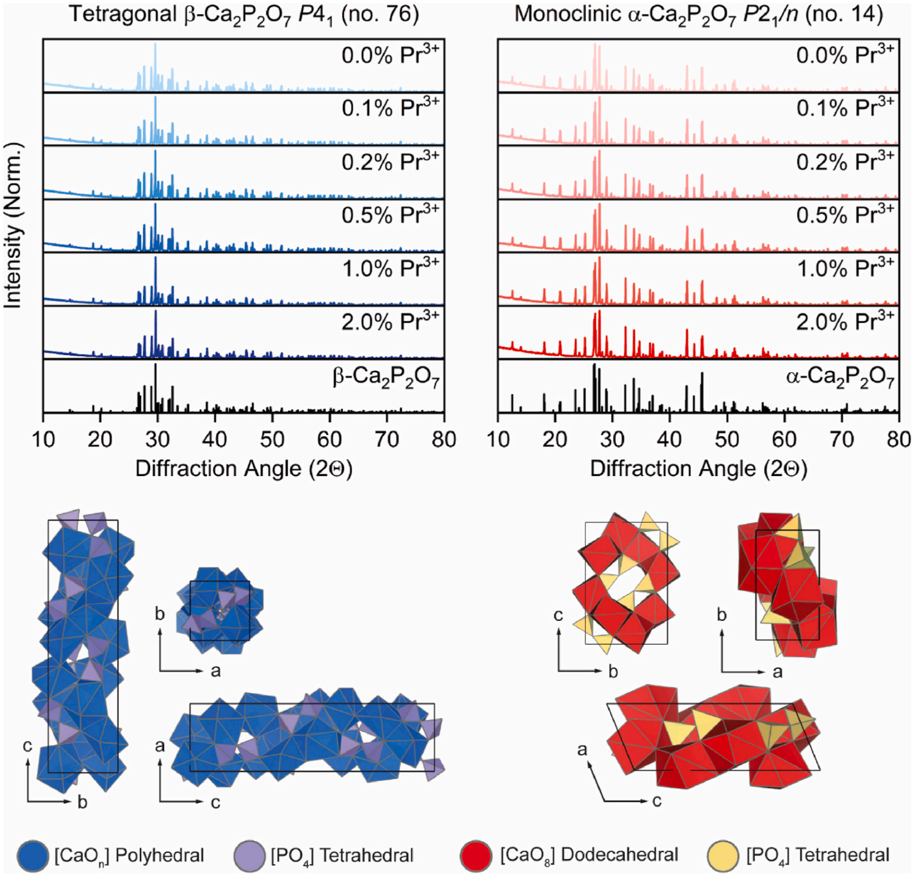

Fig. 1. PXRD patterns of the undoped and Pr^{3+}/Na^{+} substituted pyrophosphates (0.1–2.0 % Pr(III)). Samples belonging to the low-temperature β-$Ca_2P_2O_7$ phase are shown on the left and samples belonging to the high-temperature α-$Ca_2P_2O_7$ phase are shown on the right. Reference patterns were derived from data published in Refs. [2,3]. Schematic representation of the respective unit cells along the three crystal axes were drawn using *VESTA 3*.

features two distinct [P_2O_7] units which are formed by P1O_4-P2O_4 and P3O_4-P4O_4-pairs. The most significant difference between these two units is the P-O-P bond angle, being 130.5° and 137.8° respectively. Four different sites for calcium ions are found in the structure: Two (Ca1, Ca3) are coordinated sevenfold into polyhedrons that can be described as distorted pentagonal bipyramids, one (Ca4) is coordinated eightfold into a bicapped trigonal prism, and the last one (Ca2) is coordinated ninefold into a tricapped trigonal prism [2,43]. The eclipsed [P_2O_7] groups are connected to the surrounding [CaO_n] ($n = 7,8,9$) polyhedrons via shared edges and form chains along the a-axis. The monoclinic α-$Ca_2P_2O_7$ structure contains only one type of [P_2O_7] group in which the characteristic P-O-P bond angle was found to be 130° [3]. Calcium ions are surrounded by eight oxygen anions and form two types of [CaO_8] dodecahedrons that differ in their bond distances and angles.

3.2. *Diffuse reflectance and excitation spectroscopy*

Reflectance data of pristine β-$Ca_2P_2O_7$ and α-$Ca_2P_2O_7$ are presented in the supporting information (Figs. S1a and S1b). The samples exhibit high reflectance throughout the visible range down to 300 nm, below which a slight decrease in reflectance is observed likely due to crystal defects. A further decrease in reflectance, indicating a band edge, can be observed at approximately 160 nm. From these reflectance spectra, the band gap width is estimated to be around 7.75 eV, which aligns well with values reported for other phosphates [44]. Doping by Pr^{3+} results in the emergence of two line-multiplets around 450 and 600 nm (Fig. 2a and d). These lines correspond to the transitions $^3H_4 \rightarrow {}^3P_{0,1,2}, {}^1I_6$ (450 nm) and $^3H_4 \rightarrow {}^1D_2$ (600 nm) of praseodymium. Fig. 2b and e shows the respective excitation spectra of β-$Ca_2P_2O_7$:Pr(III) and α-$Ca_2P_2O_7$:Pr(III) in the VUV range. Monitoring the emission at 265 nm revealed a set of broad excitation bands ranging from 150 to 225 nm. Inspecting the excitation band closer revealed that the band can be deconstructed roughly into three distinct bands located at 165, 200, and 225 nm. The low energy bands originate from electronic transitions between the *[Xe] 4f²* ground state $^3H_4$ and the lowest *[Xe]4f¹5d¹* crystal field component. These transitions manifest as broad bands because both the ground and excited states are of different parity, rendering the transitions allowed according to the *Laporte* selection rule. The remaining band, located around 165 nm, is assigned to the band-to-band transition of the tetrahedral $[PO_4]^{3-}$ moiety of the host structure. This band location aligns well with the observed band edge in the VUV reflectance spectra. *Saito* et al. assigned the origin of these bands to the $2t_2 \rightarrow 2a,3t_2$ intramolecular transition of the $[PO_4]^{3-}$ anion [45]. Furthermore, similar band energies have been reported for other phosphates such as $LnPO_4$ (Ln = Y, La, Gd, Lu), $K_3Tb(PO_4)_2$, and $Sr_3(PO_4)_2$ [46,47]. Visibility of this host structure caused band while, monitoring the $[Xe]4f^15d^1 \rightarrow {}^3H_J$ ($J = 4,5,6$) transitions of praseodymium indicates energy transfer from the conduction band to the Pr^{3+} activator. In addition to the VUV excitation spectra monitoring the $[Xe]4f^15d^1 \rightarrow [Xe]4f^2$ emission at 265 nm excitation spectra in the same range were recorded while monitoring the $[Xe]4f^2 \rightarrow [Xe]4f^2$ emission at 598 nm ($^1D_2 \rightarrow {}^3H_4$) (s. Fig. S5). Comparison of both spectra types revealed the same combination of bands located at 160 and 200 nm. Nevertheless, it should be noted that intensities while monitoring the 598 nm emission were significantly lower. The influence of the lower count rate is also notable due to the occurrence of several spectrometer artifacts between 250 and 350 nm. This might indicate that the relaxation from the excited *5d*-states to the *4f*-states with subsequent emission from these is not favoured in

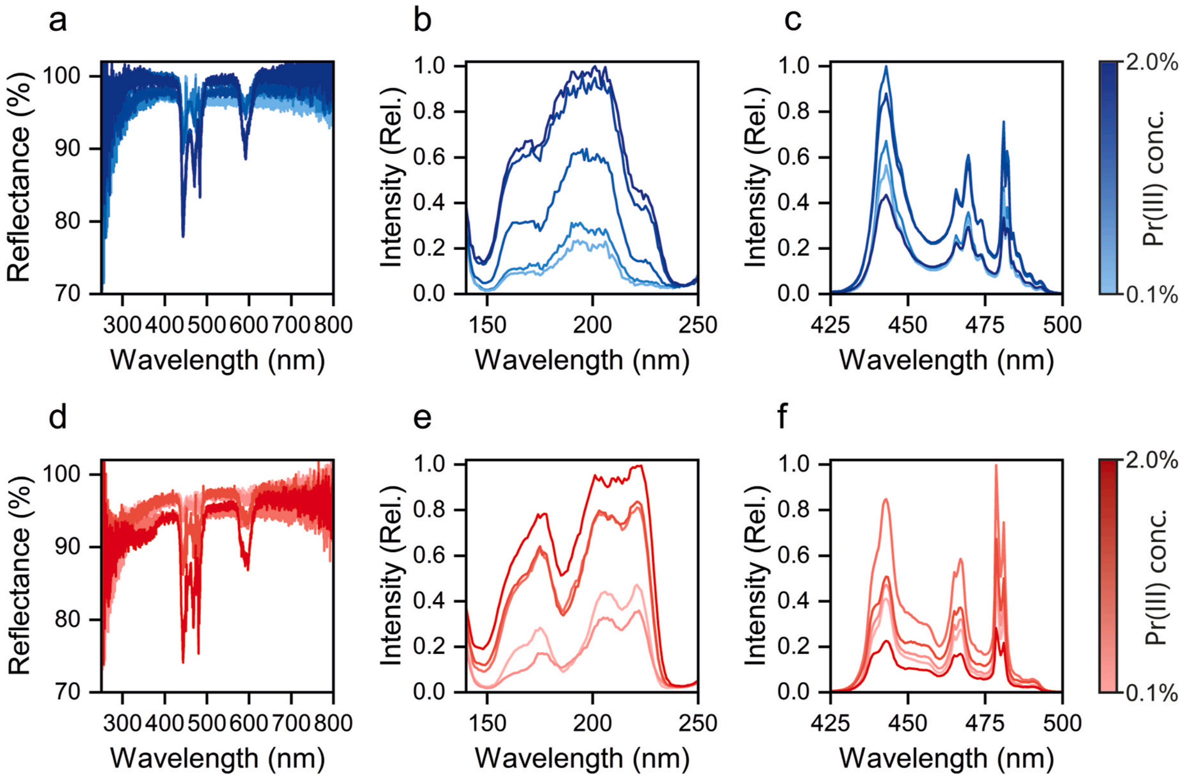

Fig. 2. Reflectance and excitation properties of α-$Ca_2P_2O_7$ (2d, 2e, 2f) and β-$Ca_2P_2O_7$ (2a, 2b, 2c) doped by Pr^{3+}. The degree of substitution ranged from 0.1 up to 2.0 %. (a) and (d) show diffuse reflectance spectra between 250 and 800 nm, measured against $BaSO_4$. (b) and (e) show the relative VUV-excitation spectra between 140 and 250 nm monitoring the $[Xe]\ 4f^1 5d^1 \rightarrow [Xe]4f^2$ emission at 265 nm. (c) and (f) show excitation spectra between 425 and 500 nm. Excitation spectra in the visible range were recorded while monitoring the 606 nm emission maximum corresponding to the $^1D_2 \rightarrow {}^3H_4$ transition of praseodymium.

comparison to direct radiative relaxation from the *5d*-states. This interpretation seems plausible when considering the quantum mechanically allowed nature of the *5d-4f* transitions and the resulting high transition probabilities.

Fig. 2c and f presents the excitation spectra of both substitution series in the visible range. Both series show the characteristic line multiplet of praseodymium extending from 445 to 500 nm. All observed excitation lines are caused by the intraconfigurational transitions inside of the Pr^{3+} $[Xe]4f^2$ electron configuration. Using the excitation spectra recorded at cryogenic temperatures (see Figs. S3a and S3b) the lines were indexed to the corresponding electron transitions in Table 1, employing the energy level data published by *Esterowitz* et al. [48]. Cooling the samples to the temperature of liquid nitrogen, limited temperature induced spectral broadening which allowed a more detailed look at the splitting of the respective $[Xe]4f^2$ states. The splitting of the lanthanide $[Xe]4f^n$ states into the energetic fine structure is well understood and governed by four effects: the *Coulomb* interaction of the electrons, the spin-orbit coupling, the crystal field or *Stark* splitting, and the *Zeeman* effect. In trivalent praseodymium these effects give rise to a maximum of 91 SLJM-terms, the actual number of sublevels in a given material depends on the local symmetry of the activator ion. Crystal field induced splitting of the ^3P_J states (J = 0,1,2) can explain the additional observed excitation lines. Expectedly, both types of excitation spectra show an intensity dependence on the activator concentration and comparison of the activator concentrations resulting in the highest excitation intensity revealed a significant difference between the intra- and interconfigurational transitions. A substitution degree of just 0.5 % proved ideal for the $[Xe]4f^2 \rightarrow [Xe]4f^2$ transitions, meanwhile 2 % showed the highest intensity for the $[Xe]4f^2 \rightarrow [Xe]4f^1 5d^1$ transitions indicating the feasibility of even higher activator concentrations.

Table 1
Observed lines and bands in the diffuse reflectance, VUV excitation (Fig. 2a and b), and 77 K excitation spectra (Fig. S3a) of β-$Ca_2P_2O_7$:Pr.

Material	Transition Type	Transition	Wavelength (nm)
β-$Ca_2P_2O_7$:Pr	Band to band	Band gap	165
	$[Xe]4f^2 \rightarrow [Xe]\ 4f^1 5d^1$	$^3H_4 \rightarrow [Xe]4f^1 5d^1$	200
		$^3H_4 \rightarrow [Xe]4f^1 5d^1$	225
	$[Xe]4f^2 \rightarrow [Xe]4f^2$	$^3H_4 \rightarrow {}^3P_2$	441
		$^3H_4 \rightarrow {}^3P_2$	443
		$^3H_4 \rightarrow {}^3P_2$	444
		$^3H_4 \rightarrow {}^1I_6$	455
		$^3H_4 \rightarrow {}^3P_1$	465
		$^3H_4 \rightarrow {}^3P_1$	469
		$^3H_4 \rightarrow {}^3P_0 \rightarrow {}^3P_1$[a]	473
		$^3H_4 \rightarrow {}^3P_0$	480
		$^3H_4 \rightarrow {}^3P_0$	482
		$^3H_4 \rightarrow {}^3P_0$	483
		$^3H_4 \rightarrow {}^3P_0$	485

[a] Transition not observed at 77 K, only at elevated temperatures.

3.3. Emission spectroscopy

The emission properties of β-$Ca_2P_2O_7$:Pr and α-$Ca_2P_2O_7$:Pr are shown in Fig. 2 and Fig. S2 of the supporting material. Upon excitation by VUV radiation at 160 nm, the spectra of β-$Ca_2P_2O_7$:Pr are dominated by two broad emission bands centred at 235 and 265 nm (see Fig. 3a). In comparison, the VUV emission spectra of α-$Ca_2P_2O_7$:Pr (Fig. 3d) show higher resolution, with the splitting of the two broad bands into four distinct bands. These bands are attributed to the allowed interconfigurational $[Xe]4f^1 5d^1 \rightarrow [Xe]4f^2$ transitions of praseodymium. The broad band nature of these transitions can be traced back to the orbital involvement of the *5d* excited state in the bonding of the activator ion. This connection yields a large ΔR value in the respective configurational coordinate diagram. The four bands centred at 229, 239, 255, 265 nm correspond to transitions from the lowest $[Xe]4f^1 5d^1$ crystal field

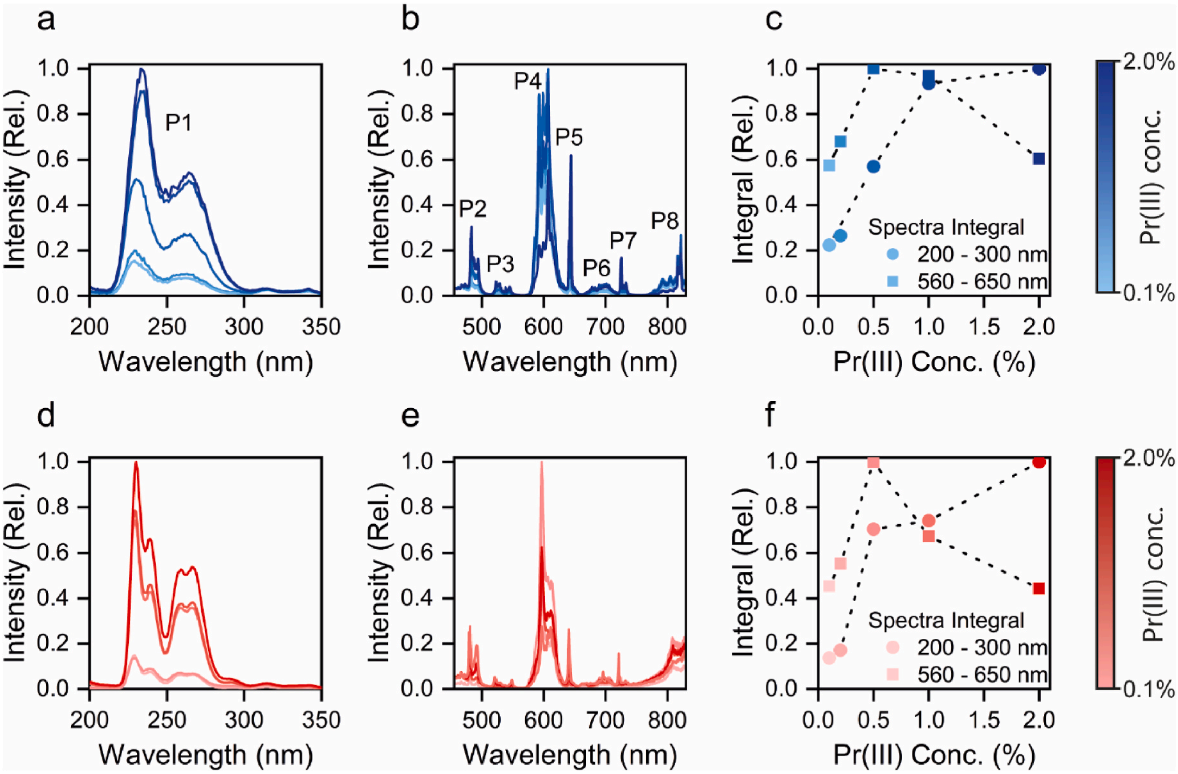

Fig. 3. Emission spectra of α- $Ca_2P_2O_7$:Pr(III) (2d, 2e, and 2f) and β-$Ca_2P_2O_7$:Pr(III) (2a, 2b, and 2c) upon excitation at various energies. The degree of substitution ranged from 0.1 to 2.0 %. (a) and (d) show emission spectra upon VUV-excitation at 160 nm ranging from 200 to 350 nm. (b) and (e) show the respective emission spectra in the visible range (450–830 nm) upon excitation via the $^3H_4 \rightarrow {}^3P_2$ (443 nm) transition of praseodymium. (c) and (f) depict several emission integrals as a function of the praseodymium concentration.

component of Pr^{3+} to low-lying *[Xe]4f²* states $^3H_{4,5,6}$ and $^3F_2$. The differences in the measured peak wavelengths are consistent with the energetic separation of the *[Xe]4f²* states as reported by *Caspers* et al. [49]. In contrast the intraconfigurational *[Xe]4f²* → *[Xe]4f²* are visible as narrow emission lines stretching from the visible to the NIR range (see Fig. 3b and e, Fig. S2a, and S2b). Using the emission spectrum at cryogenic temperature, the emission lines and bands were indexed to their respective electronic transitions and listed in Table 2. The emission spectra in the visible range are dominated by a line multiplet in the red spectral range around 600 nm (P4) corresponding to the transitions $^3P_{0,1} \rightarrow {}^3H_6$ and $^1D_2 \rightarrow {}^3H_4$ of Pr^{3+}. Notably the shape of the main emission multiplets show stark differences between the two polymorphs. The spectral differences arise as the result of the differently coordinated Ca/Pr polyhedral. Additionally, around 640 nm a narrow emission line corresponding to the $^3P_0 \rightarrow {}^3F_2$ transition is visible. This transition is known to be of hypersensitive nature, meaning the emission intensity is highly responsive to changes of the activator environment. Generally, the intensities of all *[Xe]4fⁿ* ↔ *[Xe]4fⁿ* transitions are summarized in the *Judd-Ofelt* theory under the phenomenological parameters Ω_λ ($\lambda = 2$, 4, and 6) [50,51]. Structurally, several factors have been identified which influence these Ω_λ parameters and subsequently determine the emission intensities of the hypersensitive transitions. It is well known that *[Xe]4fⁿ* ↔ *[Xe]4fⁿ* transition probabilities increase following a decrease in symmetry which is reflected in the parameter Ω_2. This effect is even stronger for the hypersensitive transitions with $\Delta J = \pm 2$ and $\Delta S = 0$ due to the relaxation of the *Laporte* selection rule following mixture of the *4f* and *5d* wavefunctions [52,53]. Early empirical observations connected the intensity of hypersensitive transitions to the covalency of the activator ligand bond [54]. This was later dismissed and improved upon: local activator symmetry was still represented by Ω_2, polarizability of the ligand by Ω_6, and the number of 4f-electrons by $\Omega_{4,6}$ [55]. In low symmetry environments without any inversion centre, emission spectra can even be dominated by such transitions and the transitions itself generally serve as an approximate judge of the local symmetry of the activator ion [56,57].

Concentration quenching, a critical characteristic of phosphor materials, describes the relationship between activator concentration and quantum yield. Generally, a high activator concentration is desirable to enhance the light output of a given light source. Increases in activator concentration are limited by activator concentration-dependent non-radiative decay mechanisms. These quenching mechanisms are predominately influenced by the interatomic distances between adjacent activator ions. Decreasing the distance between two activator ions below a threshold distance unique to the activator ions, increases the probability of energy transfer over the respective cation sub lattice to quenching centres such as point defects or the crystallite surface. In this study the concentration quenching behaviour of the calcium pyrophosphate phosphors was investigated by comparing the emission integrals of the *[Xe]4f¹5d¹* → *[Xe]4f²* and the *[Xe]4f²* → *[Xe]4f²* transitions (s. Fig. 3c and f, Fig. S2c). Similar quenching behaviour was observed for both pyrophosphate types. 0.5 % praseodymium yielded the highest emission integral for the *[Xe]4f²* → *[Xe]4f²* transitions, while no local maximum was observed for the *[Xe]4f¹5d¹* → *[Xe]4f²* emission integrals up to 2.0 % praseodymium, indicating the feasibility of higher activator concentrations to achieve efficient UV emission. It should be noted that due to the energetic position of the lowest *[Xe]4f¹5d¹* crystal field component around 43500 cm^{-1} no emission from the $^1S_0$ state at 46500 cm^{-1} is observed.

3.4. Temperature resolved spectroscopy

Temperature-resolved emission spectra of β-$Ca_2P_2O_7$:Pr (0.5 %) and α-$Ca_2P_2O_7$:Pr (0.5 %) are presented in Fig. 4a and c. Additionally, the relative emission integrals and selected line intensities are plotted in

Table 2

Observed lines and bands in the VUV emission (Figs. 3a) and 77 K emission spectra (Fig. 4a) of β-$Ca_2P_2O_7$:Pr.

Material	No.	Transition type	Transition	Wavelength (nm)
β-$Ca_2P_2O_7$:Pr	P1	$[Xe]4f^{1}5d^{1} \rightarrow [Xe]4f^{2}$	$[Xe]4f^{1}5d^{1} \rightarrow {}^{3}H_{4}$	229
			$[Xe]4f^{1}5d^{1} \rightarrow {}^{3}H_{5}$	239
			$[Xe]4f^{1}5d^{1} \rightarrow {}^{3}H_{6}$	258
			$[Xe]4f^{1}5d^{1} \rightarrow {}^{3}F_{2}$	265
	P2	$[Xe]4f^{2} \rightarrow [Xe]4f^{2}$	${}^{3}P_{2,1,0} \rightarrow {}^{3}H_{4}$	481
				483
				484
				486
				490
				493
	P3		${}^{3}P_{1} \rightarrow {}^{3}H_{5}$[a]	522
				525
				528
			${}^{3}P_{0} \rightarrow {}^{3}H_{5}$	538
				541
				544
				550
	P4		${}^{3}P_{1} \rightarrow {}^{3}H_{6}$[a]	585
				592
				594
			${}^{1}D_{2} \rightarrow {}^{3}H_{4}$	599
				600
				603
				607
				609
			${}^{3}P_{0} \rightarrow {}^{3}H_{6}$	612
				616
	P5		${}^{3}P_{0} \rightarrow {}^{3}F_{2}$	640
				643
	P6		${}^{1}D_{2} \rightarrow {}^{3}H_{5}$	689
			${}^{3}P_{0} \rightarrow {}^{3}F_{3}$	693
				700
				709
	P7		${}^{3}P_{0} \rightarrow {}^{3}F_{4}$	724
				725
				727
				729
				733
	P8		${}^{1}D_{2} \rightarrow {}^{3}H_{6}$	791
				803
				806
				813
				816
				821
	P9		${}^{3}P_{0} \rightarrow {}^{1}G_{4}$	859
				879
	P10		${}^{1}D_{2} \rightarrow {}^{3}F_{4}$	994
				1014
				1044
	P11		${}^{1}D_{2} \rightarrow {}^{1}G_{4}$	1422–1500

[a] Transition not observed at 77 K, only at elevated temperatures.

Fig. 4b and d. The respective temperature-dependent excitation spectra are provided in the supporting information (Figs. S3a and S 3b). Both the excitation and emission spectra consist of the previously discussed intraconfigurational $[Xe]4f^{2} \leftrightarrow [Xe]4f^{2}$ transitions of praseodymium. Within the investigated temperature range, an overall decrease of the luminous intensity is observed for both materials, a phenomenon known as thermal quenching. The parameter $T_{1/2}$, which describes the relative change of emission intensity with increasing temperature, is crucial for comparing different phosphor materials. The thermal quenching temperature was calculated using Eq. (1). In this context, I(T) represents the emission intensity at a given temperature T, while I(0) denotes the emission intensity without any thermal quenching. B is a fitting parameter, k_B is the Boltzmann constant (1.38×10^{23} J K^{-1}), and E_A is the activation energy required to bridge the energy barrier to the non-radiative decay pathways.

$$I(T) = \frac{I(0)}{1 + B\exp\left(\frac{-E_A}{k_B T}\right)} \tag{1}$$

For both phosphors the relative emission integrals (560–650 nm) of the line multiplet corresponding to the $[Xe]4f^{2} \rightarrow [Xe]4f^{2}$ transitions ${}^{2}D_{1} \rightarrow {}^{3}H_{4}$ and ${}^{3}P_{0} \rightarrow {}^{3}H_{6}$ in the red spectral are plotted and fitted using Eq. (1). From the fit, $T_{1/2}$ values of 749 and 722 K were determined with rather high standard deviations of 23 and 22 K. Additionally the relative line intensity at 642 nm (${}^{3}P_{0} \rightarrow {}^{3}F_{2}$) is plotted as a comparison. It is possible to use the line intensities since the $[Xe]4f^{2} \rightarrow [Xe]4f^{2}$ emission lines barely show any temperature induced spectral shift. Fitting of the line intensities resulted in $T_{1/2}$ values of 235 K (±5 K) K for β-$Ca_2P_2O_7$:Pr and 330 K (±5 K) for α-$Ca_2P_2O_7$:Pr. The deviation can be explained by the disregard of the line intensities for any spectral broadening, the emission integrals on the other hand show the temperature induced spectral broadening of the emission lines. Overall, the luminescence of Pr^{3+} shows slightly higher temperature stability in the α-$Ca_2P_2O_7$ host as can be seen from the set in of integral decrease only above 200 K. Close inspection of the temperature dependent excitation and emission spectra revealed the emergence of new excitation and emission lines which don't follow the standard thermal quenching behaviour. The relative line intensity of β-$Ca_2P_2O_7$:Pr at 592 nm is plotted in Fig. 4b. The intensity of the emission first increases with increasing temperature and only shows classic thermal quenching after reaching at maximum intensity at 225 K. Such appearances of new emission lines are quite common and are caused by thermal population of a higher energy state. In the case of Pr^{3+}, the small energetic gap of ~600 cm^{-1} between the ${}^{3}P_{0}$ and the ${}^{3}P_{1}$ states can be bridged by electrons in the excited ${}^{3}P_{0}$ state through the input of thermal energy. Accordingly, emission from the thermally excited ${}^{3}P_{1}$ states can be observed. The newly observed emission lines at ~524 nm, ~592 nm, and ~680 nm can therefore be assigned to the following intraconfigurational transitions ${}^{3}P_{1} \rightarrow {}^{3}H_{5}$, ${}^{3}P_{1} \rightarrow {}^{3}H_{6}$, and ${}^{3}P_{1} \rightarrow {}^{3}F_{3}$. Similar line intensity patterns are observable in the respective temperature dependent excitation spectra where an additional excitation line is observed at 473 nm corresponding to the thermal ${}^{3}P_{0} \rightarrow {}^{3}P_{1}$ population. Exploitation of this temperature dependent behaviour has been suggested and realised in praseodymium based optical thermometers [58].

3.5. Time resolved spectroscopy

Fig. 5 shows the results of the time dependent photoluminescence measurements of the two substitution series β-$Ca_2P_2O_7$:Pr and α-$Ca_2P_2O_7$:Pr (0.1–2.0 %) at room temperature. The decay curves were recorded upon 443 nm excitation while monitoring the 598 nm emission maximum. The decay curves were fitted using Eq. (2) wherein I(t) presents the emission intensity at a point in time t, A_n is a dimensionless fitting parameter, and τ_n the partial decay time. Starting from the partial decay time the overall average decay times were calculated by applying Eq. (3). Here τ_n are the partial decay times and A_n the respective fractions.

$$I(t) = A_0 + A_1 e^{-t/\tau_1} + A_2 e^{-t/\tau_2} + A_n e^{-t/\tau_n} \tag{2}$$

$$\tau = \frac{A_1\tau_1^2 + A_2\tau_2^2}{A_1\tau_1 + A_2\tau_2} \tag{3}$$

The plotted decay times of α-$Ca_2P_2O_7$:Pr and β-$Ca_2P_2O_7$:Pr in Fig. 5c show the continuous decrease of the decay times with increasing activator concentration. In the low concentration range (0.1 and 0.2 %) the decay times of both materials are stable at around 190 and 300 μs, for β-, and α-phase respectively. Overall the decay times of the β-$Ca_2P_2O_7$:Pr phosphors are slightly lower than those of the α-$Ca_2P_2O_7$:Pr materials

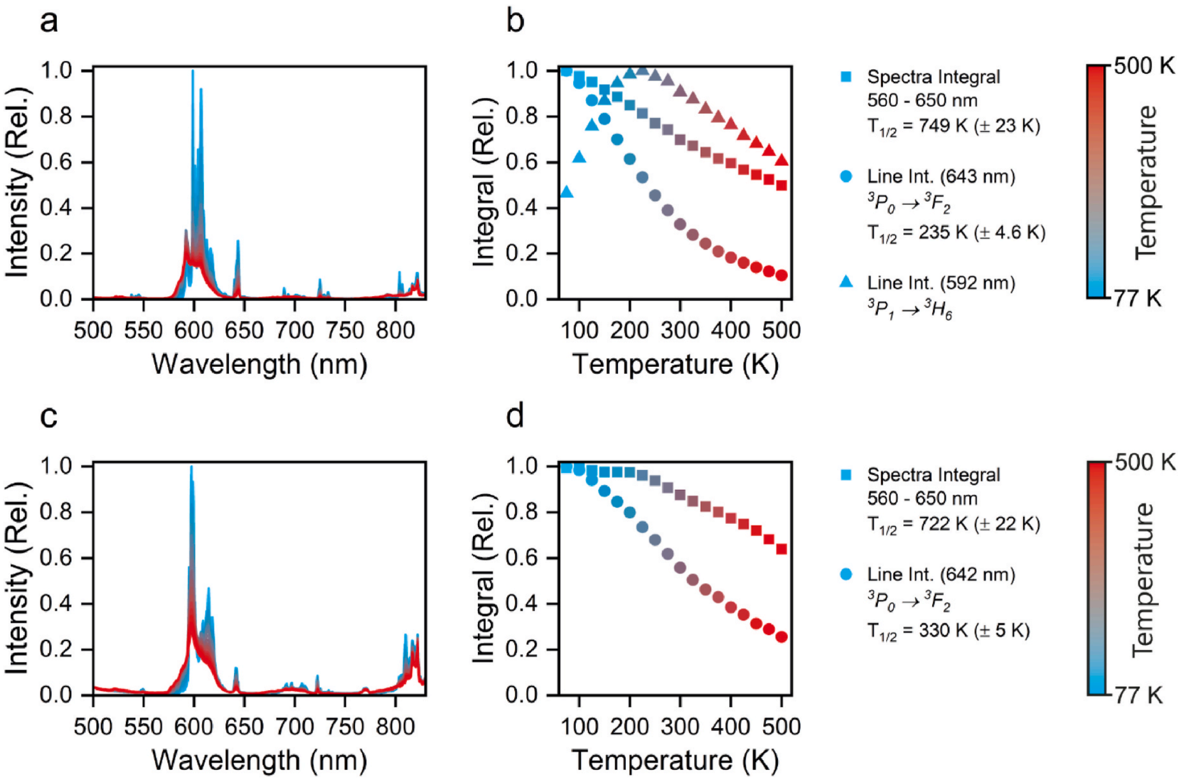

Fig. 4. Temperature dependent emission spectra of the two pyrophosphate polymorphs. (a) and (b) show the spectroscopic data of β-$Ca_2P_2O_7$:Pr(III), meanwhile (c) and (d) show the data of α-$Ca_2P_2O_7$:Pr(III). Doping concentration was chosen at 0.5 % for both substances. The spectra were recorded in a temperature range from 77 to 500 K in 25 K steps. (a) and (c) show the emission spectra excited at 443 via the $^3H_4 \rightarrow {}^3P_2$ transition of praseodymium while the respective relative emission integrals and intensities are shown in (b) and (d).

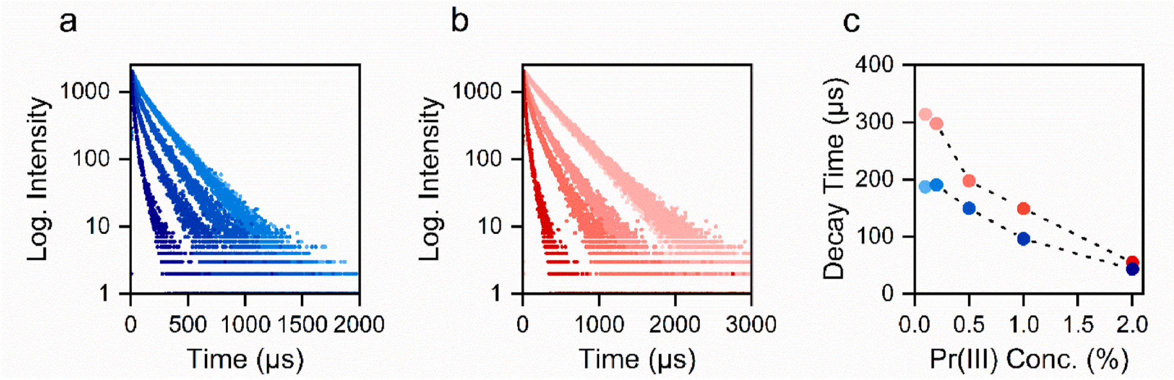

Fig. 5. Decay time measurements of α-, and β-$Ca_2P_2O_7$:Pr(III) (0.1–2.0 %). The decay curves were recorded upon 443 nm excitation ($^3H_4 \rightarrow {}^3P_2$) while monitoring the emission line at 598 nm ($^1D_2 \rightarrow {}^3H_4$). (a) and (b) show the decay curves of β-$Ca_2P_2O_7$:Pr(III) and α-$Ca_2P_2O_7$:Pr(III) respectively, (c) presents the respective average decay times.

being around. The decrease of the decay times is in line with the observed concentration quenching of the *[Xe]4f*^{2} → *[Xe]4f*^{2} emission. Contributions to the average decay times from fast non-radiative quenching pathways reduces the average decay time. Decay curves of β-$Ca_2P_2O_7$:Pr were fitted using a bi-exponential fit at 0.1 and 0.2 % and a tri-exponential fit at higher substitution degrees. While the decay curves of α-$Ca_2P_2O_7$:Pr required a mono-exponential fit at 0.1 and 0.2 % and a bi-exponential fit at higher praseodymium concentrations. The calculated decay times are listed in Table 3.

Generally, non-mono-exponential decay behaviour indicates the existence of several distinct praseodymium species with each species showing a distinct decay behaviour. In first approximation this is the result of several differently coordinated praseodymium ions, other

Table 3
Exponential fits and calculated decay times of the α- and β-$Ca_2P_2O_7$:Pr^{3+} (0.1–2.0 %) sample series. The standard deviations are given in parentheses.

Pr^{3+}-Conc./%	β-$Ca_2P_2O_7$		α-$Ca_2P_2O_7$	
	Decay time/μs	Fit	Decay time/μs	Fit
0.1	187.12 (3)	Bi-exp.	313.8 (1)	Mono-exp.
0.2	190.56 (3)	Bi-exp.	297.5 (2)	Mono-exp.
0.5	149.33 (3)	Tri-exp.	197.9 (2)	Bi-exp.
1.0	96.33 (3)	Tri-exp.	148.7 (1)	Bi-exp.
2.0	43.47 (1)	Tri-exp.	55.2 (1)	Bi-exp.

explanations can be the existence of activator species that are locally clustered or that are located near the crystallite surface. In the case of the pyrophosphates the praseodymium ions are expected to occupy the Ca-polyhedral. As four different Ca-sites are found in the β-$Ca_2P_2O_7$:Pr structure, the results of the time-dependent photoluminescence measurements can be connected to the structural data via the occupation of further Ca-sites with increasing activator concentration. This also aligns nicely with results on the α-$Ca_2P_2O_7$ materials, in which only two different Ca-sites (CN = 8) with varying bond distances and angles are found. Here at a low Pr(III) concentration only one of the two dodecahedral sites is occupied resulting in the observation of mono-exponential decay. Upon further praseodymium incorporation the second Ca-site is increasingly occupied resulting in a second decay constant and overall, a bi-exponential decay behaviour.

3.6. Phase comparison

Fig. 6 shows direct comparison of the emission properties of the two polymorphs. A qualitative comparison of the main emission multiplett in the red spectral range is shown in Fig. 6a. The observed emission lines can be attributed to the previously mentioned intraconfigurational transitions $^1D_2 \rightarrow {}^3H_4$, $^3P_0 \rightarrow {}^3H_6$ (600–625 nm) and the hypersensitive transition $^3P_0 \rightarrow {}^3F_2$. Due to the different coordination environments of the Pr^{3+} species in the two polymorphs the crystal field splitting of the states will differ. Deconvolution into the crystal field components is hindered by the spectral overlap of the individual lines. Furthermore, the ration of the hypersensitive $^3P_0 \rightarrow {}^3F_2$ transition to the normal $^1D_2 \rightarrow {}^3H_4$ and $^3P_0 \rightarrow {}^3H_6$ transitions (Fig. 6a) is of interest. As the intensity of the hypersensitive transition in the β-$Ca_2P_2O_7$ material exceeds that of the α-$Ca_2P_2O_7$ phase this could indicate higher symmetry of the Pr^{3+} species in β-$Ca_2P_2O_7$. Due to the strong symmetry dependence of the hypersensitive transition intensities such ratios are often employed to judge the symmetry of lanthanide doped materials but is most commonly used in Eu^{3+} activated materials [59,60]. Direct comparison of the $[Xe]4f^15d^1 \rightarrow [Xe]4f^2$ transitions (Fig. 6b) revealed a higher emission intensity for the α-$Ca_2P_2O_7$:Pr^{3+} phosphors, with β-$Ca_2P_2O_7$:Pr^{3+} showing less than 60 % of the $Ca_2P_2O_7$:Pr^{3+}. This observation can be explained by considering the crystal chemistry and especially the site symmetry of the different Ca^{2+}-sites in the two materials. Pr^{3+} occupies in the slightly less symmetrical dodecahedral site in the α-$Ca_2P_2O_7$ material. The three Ca^{2+} ions of the β-$Ca_2P_2O_7$ structure have site symmetries of D_{5h} and D_{3h} and therefore exhibited a slightly higher degree of ordering than the α-$Ca_2P_2O_7$ Ca sites with D_{2d} site symmetry. Generally, transitions probabilities of electric dipole transitions increase following a decrease in coordination symmetry. For the $[Xe]4f^2 \rightarrow [Xe]4f^2$ emission intensities a different trend is observed, here the β-$Ca_2P_2O_7$:Pr^{3+} phosphors show a more intense emission upon 443 nm excitation. The previously established structure-property relation would suggest a similar observation here. An explanation might be the differences in excitability at 443 nm. The respective excitation spectra reveal that β-$Ca_2P_2O_7$:Pr^{3+} shows higher excitability at 443 nm than α-$Ca_2P_2O_7$:Pr^{3+} which is better at 485 nm. These inconsistencies in the structure-property relationship may require further research, as a full analysis of the site occupations and the subsequent correlations of the optical properties are beyond the scope of this paper.

4. Conclusion

In this study, twelve single-phase calcium pyrophosphate ($Ca_2P_2O_7$) samples were synthesized using a solid-state method. The samples were divided into two different solid solutions, where the $Ca_2P_2O_7$ host materials was gradually substituted with trivalent praseodymium (Pr^{3+}) in concentrations ranging from 0.1 % to 2.0 %. The investigation focused on comparing the tetragonal β-$Ca_2P_2O_7$ and the monoclinic α-$Ca_2P_2O_7$, which are two of its three known polymorphs. Inclusion of P_2O_5 as volatile additive in the annealing process enabled the reproducible synthesis of single phase α-$Ca_2P_2O_7$ samples. The luminescence properties, dependent on activator concentration, were studied using various spectroscopic methods at room temperature. The wide band gap of the phosphate host material allows efficient and broad UV emission bands, along with typical narrow lanthanide emission lines. Emission bands in the UV-C range (235 and 265 nm) were attributed to interconfigurational $[Xe]4f^15d^1 \rightarrow [Xe]4f^2$ transitions, with the optimal activator concentration identified as 2 %. The narrow emission lines in the visible and infrared range were assigned to $[Xe]4f^2 \rightarrow [Xe]4f^2$ transitions. In the visible spectrum, the emission was dominated by a multiplet around 600 nm, which was resolved into the $^1D_2 \rightarrow {}^3H_4$ and $^3P_{0,1} \rightarrow {}^3H_6$ transitions. A local maximum for $[Xe]4f^2 \rightarrow [Xe]4f^2$ transitions was observed at 0.5 % Pr^{3+}. Additionally, the thermal quenching of both pyrophosphate polymorphs was investigated in the temperature range from 77 to 500 K. From the respective emission integrals $T_{1/2}$ values exceeding 700 K were determined. Furthermore, the emergence of new emission lines was observed with increasing temperature. These could be assigned to transitions relaxing from the $^3P_1$ excited state and are therefore the result of thermal population from the $^3P_0$ state into the $^3P_1$ state. Direct comparison of the emission properties showed that β-$Ca_2P_2O_7$:Pr showed roughly 60 % emission intensity of the α-$Ca_2P_2O_7$:Pr phosphor in the UV range (Fig. 6b). On the contrary the $[Xe]4f^2 \rightarrow [Xe]4f^2$ transitions showed higher intensities in the β-$Ca_2P_2O_7$:Pr materials (Fig. 6c–Fig. S2c). Considering the efficient UVC emission in the spectral range relevant for the inactivation of microorganisms and the excellent biocompatibility of the host material these materials might be

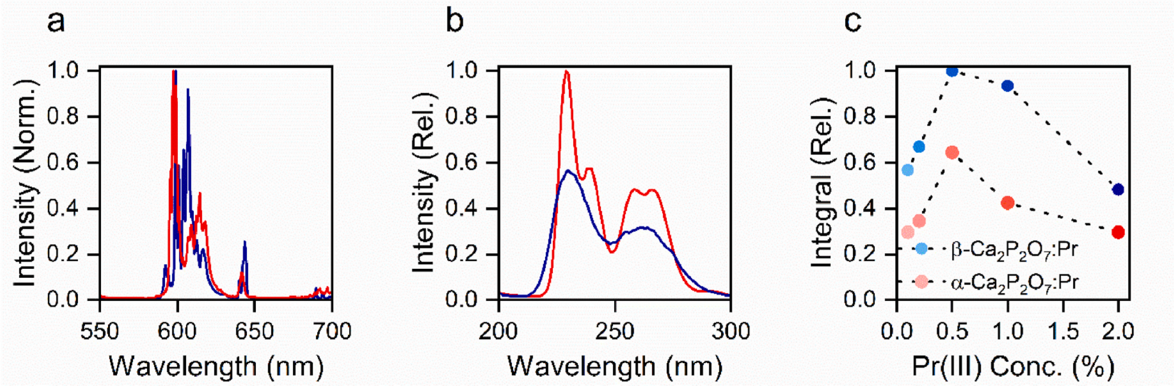

Fig. 6. Comparison of the emission properties of the Pr^{3+} doped $Ca_2P_2O_7$ polymorphs. Data of α-$Ca_2P_2O_7$ and β-$Ca_2P_2O_7$ in red and blue respectively. (a) Emission spectra in the visible range upon 443 nm excitation at 77 K (0.5 % Pr^{3+}). (b) Room temperature VUV emission spectra upon 160 nm excitation (2.0 % Pr^{3+}). (c) Relative emission integrals of the $[Xe]4f^2 \rightarrow [Xe]4f^2$ emission in the red spectral range (560–650 nm), α-$Ca_2P_2O_7$:Pr and β-$Ca_2P_2O_7$:Pr^{3+} in comparison (λ_{Ex} = 443 nm).

interesting as additives in bone cements or as coatings onto prosthesis.

CRediT authorship contribution statement

Tim Pier: Writing – original draft, Visualization, Project administration, Investigation, Formal analysis, Data curation. **Franziska Schröder:** Investigation. **Jan Kappelhoff:** Investigation. **Julia Hopster:** Investigation. **Thomas Jüstel:** Writing – review & editing, Supervision, Resources, Funding acquisition, Conceptualization.

Declaration of competing interest

The authors declare the following financial interests/personal relationships which may be considered as potential competing interests: Tim Pier reports financial support was provided by Ministry of Culture and Science of the State of North Rhine-Westphalia, Germany. If there are other authors, they declare that they have no known competing financial interests or personal relationships that could have appeared to influence the work reported in this paper.

Data availability

Data will be made available on request.

Acknowledgements

The authors are grateful to the Ministry of Culture and Science of the State of North Rhine-Westphalia, Germany for generous financial support.

Appendix A. Supplementary data

Supplementary data to this article can be found online at https://doi.org/10.1016/j.jlumin.2024.120934.

References

[1] G. Lohmüller, G. Schmidt, B. Deppisch, V. Gramlich, C. Scheringer, Die Kristallstrukturen von Yttrium-Vanadat, Lutetium-Phosphat und Lutetium-Arsenat, Acta Cryst. B 29 (1973) 141–142, https://doi.org/10.1107/S0567740873002098.

[2] N.C. Webb, The crystal structure of β-$Ca_2P_2O_7$, Acta Cryst 21 (1966) 942–948, https://doi.org/10.1107/S0365110X66004225.

[3] C. Calvo, The crystal structure of α-$Ca_2P_2O_7$, Inorg. Chem. 7 (1968) 1345–1351, https://doi.org/10.1021/ic50065a019.

[4] D.E.C. Corbridge, The crystal structure of sodium triphosphate, $Na_5P_3O_{10}$, phase I, Acta Cryst 13 (1960) 263–269, https://doi.org/10.1107/S0365110X60000583.

[5] H.M. Ondik, The structure of anhydrous sodium trimetaphosphate $Na_3P_3O_9$, and the monohydrate, $Na_3P_3O_9.H_2O$, Acta Cryst 18 (1965) 226–232, https://doi.org/10.1107/S0365110X65000518.

[6] A.J. Wojtowicz, D. Wenewski, A. Lempicki, L.A. Boatner, Scintillation mechanisms in rare earth orthophosphates, Radiat. Eff. Defect Solids 135 (1995) 305–310, https://doi.org/10.1080/10420159508229856.

[7] Y.-P. Fang, A.-W. Xu, R.-Q. Song, H.-X. Zhang, L.-P. You, J.C. Yu, H.-Q. Liu, Systematic synthesis and characterization of single-crystal lanthanide orthophosphate nanowires, J. Am. Chem. Soc. 125 (2003) 16025–16034, https://doi.org/10.1021/ja037280d.

[8] F.T. Rabouw, S.A. den Hartog, T. Senden, A. Meijerink, Photonic effects on the Förster resonance energy transfer efficiency, Nat. Commun. 5 (2014) 3610, https://doi.org/10.1038/ncomms4610.

[9] M.J.J. Mangnus, J. Zom, T.A.J. Welling, A. Meijerink, F.T. Rabouw, Finite-Size effects on energy transfer between dopants in nanocrystals, ACS Nanosci. Au 2 (2022) 111–118, https://doi.org/10.1021/acsnanoscienceau.1c00033.

[10] T. Jüstel, P. Huppertz, W. Mayr, D.U. Wiechert, Temperature-dependent spectra of YPO_4:me (Me=Ce, Pr, Nd, Bi), J. Lumin. 106 (2004) 225–233, https://doi.org/10.1016/j.jlumin.2003.10.004.

[11] N. Hashimoto, Y. Takada, K. Sato, S. Ibuki, Green-luminescent (La,Ce)PO_4:Tb phosphors for small size fluorescent lamps, J. Lumin. 48–49 (1991) 893–897, https://doi.org/10.1016/0022-2313(91)90265-W.

[12] P. Gras, N. Ratel-Ramond, S. Teychéné, C. Rey, E. Elkaim, B. Biscans, S. Sarda, C. Combes, Structure of the calcium pyrophosphate monohydrate phase ($Ca_2P_2O_7 \cdot H_2O$): towards understanding the dehydration process in calcium pyrophosphate hydrates, Acta Cryst. C 70 (2014) 862–866, https://doi.org/10.1107/S2053229614017446.

[13] D. Griesiute, J. Gaidukevic, A. Zarkov, A. Kareiva, Synthesis of β-$Ca_2P_2O_7$ as an adsorbent for the removal of heavy metals from water, Sustainability 13 (2021) 7859, https://doi.org/10.3390/su13147859.

[14] E.G. Komarova, M.B. Sedelnikova, A.M. Kondranova, S.O. Kazantsev, Y. P. Sharkeev, Development of calcium phosphate coatings with regulated porous structure as drug carrier systems, J. Phys.: Conf. Ser. 1281 (2019) 12037, https://doi.org/10.1088/1742-6596/1281/1/012037.

[15] M. Nagai, T. Matsumoto, T. Matsuda, O. Ogawa US7658791B2.

[16] T. Kitsugi, T. Yamamuro, T. Nakamura, S. Kotani, T. Kokubo, H. Takeuchi, Four calcium phosphate ceramics as bone substitutes for non-weight-bearing, Biomaterials 14 (1993) 216–224, https://doi.org/10.1016/0142-9612(93)90026-X.

[17] H.C. Schweizer US2112247.

[18] F.H. Lin, C.J. Liao, K.S. Chen, J.S. Sun, H.C. Liu, Degradation behaviour of a new bioceramic: $Ca_2P_2O_7$ with addition of $Na_4P_2O_7 \cdot 10H_2O$, Biomaterials 18 (1997) 915–921, https://doi.org/10.1016/S0142-9612(97)00016-1.

[19] W. He, Y. Xie, Q. Xing, P. Ni, Y. Han, H. Dai, Sol-gel synthesis of biocompatible Eu^{3+}/Gd^{3+} co-doped calcium phosphate nanocrystals for cell bioimaging, J. Lumin. 192 (2017) 902–909, https://doi.org/10.1016/j.jlumin.2017.08.033.

[20] A.D. Anastasiou, M. Nerantzaki, A.P. Brown, A. Jha, D.N. Bikiaris, Drug loading capacity of microporous β-pyrophosphate crystals, Mater. Des. 168 (2019) 107661, https://doi.org/10.1016/j.matdes.2019.107661.

[21] A. Adamiano, V.M. Wu, F. Carella, G. Lamura, F. Canepa, A. Tampieri, M. Iafisco, V. Uskoković, Magnetic calcium phosphates nanocomposites for the intracellular hyperthermia of cancers of bone and brain, Nanomedicine (Lond.) 14 (2019) 1267–1289, https://doi.org/10.2217/nnm-2018-0372.

[22] Z. Hao, J. Zhang, X. Zhang, X. Sun, Y. Luo, S. Lu, X.-J. Wang, White light emitting diode by using α-$Ca_2P_2O_7$:Eu^{2+}, Mn^{2+} phosphor, Appl. Phys. Lett. 90 (2007) 261113, https://doi.org/10.1063/1.2752725.

[23] Z. Hao, J. Zhang, X. Zhang, S. Lu, Y. Luo, X. Ren, X. Wang, Phase dependent photoluminescence and energy transfer in $Ca_2P_2O_7$:Eu^{2+}, Mn^{2+} phosphors for white LEDs, J. Lumin. 128 (2008) 941–944, https://doi.org/10.1016/j.jlumin.2007.11.035.

[24] D. Griesiute, E. Garskaite, A. Antuzevics, V. Klimavicius, V. Balevicius, A. Zarkov, A. Katelnikovas, D. Sandberg, A. Kareiva, Synthesis, structural and luminescent properties of Mn-doped calcium pyrophosphate ($Ca_2P_2O_7$) polymorphs, Sci. Rep. 12 (2022) 7116, https://doi.org/10.1038/s41598-022-11337-y.

[25] X. Yu, Z. Wang, Q. wang, X. Mi, Warm white emission of $Ca_2P_2O_7$:Dy^{3+}, Eu^{3+} phosphor via hydrothermal method, J. Alloys Compd. 897 (2022) 162745, https://doi.org/10.1016/j.jallcom.2021.162745.

[26] J. Roman-Lopez, I.B. Lozano, E. Cruz-Zaragoza, J.I.G. Castañeda, J.A.I. Díaz-Góngora, Synthesis of β-$Ca_2P_2O_7$:Tb^{3+} to gamma radiation detection by thermoluminescence, Appl. Radiat. Isot. 124 (2017) 44–48, https://doi.org/10.1016/j.apradiso.2017.03.004.

[27] F.W. Mo, R.F. Wang, Y.W. Lan, L.Y. Zhou, T. He, X.M. Xu, Synthesis and luminescent properties of $M_2P_2O_7$:Eu^{3+} (M = Ca, Sr, Ba) phosphors, Adv. Mater. Res. 399–401 (2011) 978–981, https://doi.org/10.4028/www.scientific.net/AMR.399-401.978.

[28] R.L. Kohale, K.N. Shinde, K. Park, S.J. Dhoble, Synthesis and luminescence properties of Eu^{2+} activated $Ca_2P_2O_7$ pyrophosphate phosphor, J. Nanosci. Nanotechnol. 14 (2014) 5976–5978, https://doi.org/10.1166/jnn.2014.8313.

[29] A.M. Srivastava, Inter- and intraconfigurational optical transitions of the Pr^{3+} ion for application in lighting and scintillator technologies, J. Lumin. 129 (2009) 1419–1421, https://doi.org/10.1016/j.jlumin.2009.01.041.

[30] A.M. Srivastava, Aspects of Pr^{3+} luminescence in solids, J. Lumin. 169 (2016) 445–449, https://doi.org/10.1016/j.jlumin.2015.07.001.

[31] T.A. Tran, J. Kappelhoff, T. Jüstel, R.R. Anderson, M. Purschke, UV emitting nanoparticles enhance the effect of ionizing radiation in 3D lung cancer spheroids, Int. J. Radiat. Biol. 98 (2022) 1484–1494, https://doi.org/10.1080/09553002.2022.2027541.

[32] S. Espinoza, M.-F. Volhard, H. Kätker, H. Jenneboer, A. Uckelmann, M. Haase, M. Müller, M. Purschke, T. Jüstel, Deep ultraviolet emitting scintillators for biomedical applications: the hard way of downsizing $LuPO_4$:Pr^{3+}, Part. Part. Syst. Charact. 35 (2018) 1800282 https://doi.org/10.1002/ppsc.201800282.

[33] J. Caiut, S. Lechevallier, J. Dexpert-Ghys, B. Caillier, P. Guillot, UVC emitting phosphors obtained by spray pyrolysis, J. Lumin. 131 (2011) 628–632, https://doi.org/10.1016/j.jlumin.2010.11.004.

[34] K. Momma, F. Izumi, VESTA 3 for three-dimensional visualization of crystal, volumetric and morphology data, J. Appl. Cryst. 44 (2011) 1272–1276, https://doi.org/10.1107/S0021889811038970.

[35] T.N. Nurakhmetov, T.T. Alibay, K.B. Zhangylyssov, A.S. Nurpeissov, S. Pazylbek, D. Griesiute, A. Zarkov, A. Kareiva, Luminescence and electron–hole-trapping centers in α-$Ca_2P_2O_7$−Mn, Crystals 14 (2024) 406, https://doi.org/10.3390/cryst14050406.

[36] J.H. Welch, W. Gutt, High-temperature studies of the system calcium oxide-phosphorus pentoxide, J. Chem. Soc. (1961) 4442–4444.

[37] T. Nagai, Y. Tanaka, M. Maeda, Thermodynamic measurement of di-calcium phosphate, Metall. Mater. Trans. B 42 (2011) 685–691, https://doi.org/10.1007/s11663-011-9509-2.

[38] T. Nagai, M. Miyake, M. Maeda, Thermodynamic measurement of calcium phosphates by double knudsen cell mass spectrometry, Metall. Mater. Trans. B 40 (2009) 544–549, https://doi.org/10.1007/s11663-009-9242-2.

[39] D. Griesiute, E. Raudonyte-Svirbutaviciene, A. Kareiva, A. Zarkov, The influence of annealing conditions on the Ca/P ratio and phase transformations in bulk calcium phosphates, CrystEngComm 24 (2022) 1166–1170, https://doi.org/10.1039/d1ce01625c.

[40] W. Sauskojus, J.K. Wied, C.F. Litterscheid, M. Mangstl, J. Schmedt auf der Günne, Crystal structure of γ-$Ca_2P_2O_7$, Z. Anorg. Allg. Chem. 648 (2022) e202200196, https://doi.org/10.1002/zaac.202200196.

[41] W. Bouchelaghem, M.R. Benloucif, M. Mayoufi, A. Benmoussa, K.J. Schenk, Reinvestigation of cadmium diphosphate, Acta Cryst. E 62 (2006) i99–i102, https://doi.org/10.1107/S1600536806008397.

[42] J.-J. Bian, D.-W. Kim, K.-S. Hong, Phase transformation and sintering behavior of $Ca_2P_2O_7$, Mater. Lett. 58 (2004) 347–351, https://doi.org/10.1016/S0167-577X(03)00498-1.

[43] S. Boudin, A. Grandin, M.M. Borel, A. Leclaire, B. Raveau, Redetermination of the β-$Ca_2P_2O_7$ structure, Acta Cryst. C 49 (1993) 2062–2064, https://doi.org/10.1107/s0108270193005608.

[44] E. Nakazawa, F. Shiga, Vacuum ultraviolet luminescence-excitation spectra of RPO_4:Eu^{3+} (R = Y, La, Gd and Lu), J. Lumin. 15 (1977) 255–259, https://doi.org/10.1016/0022-2313(77)90024-2.

[45] S. Saito, K. Wada, R. Onaka, Vacuum ultraviolet reflection spectra of KDP and ADP, J. Phys. Soc. Jpn. 37 (1974) 711–715, https://doi.org/10.1143/JPSJ.37.711.

[46] H. Liang, Y. Tao, Q. Su, S. Wang, VUV–UV photoluminescence spectra of strontium orthophosphate doped with rare earth ions, J. Solid State Chem. 167 (2002) 435–440, https://doi.org/10.1006/jssc.2002.9651.

[47] C.-H. Kim, I.-E. Kwon, C.-H. Park, Y.-J. Hwang, H.-S. Bae, B.-Y. Yu, C.-H. Pyun, G.-Y. Hong, Phosphors for plasma display panels, J. Alloys Compd. 311 (2000) 33–39, https://doi.org/10.1016/S0925-8388(00)00856-2.

[48] L. Esterowitz, F.J. Bartoli, R.E. Allen, D.E. Wortman, C.A. Morrison, R.P. Leavitt, Energy levels and line intensities of Pr^{3+} in $LiYF_4$, Phys. Rev. B 19 (1979) 6442–6455, https://doi.org/10.1103/PhysRevB.19.6442.

[49] H.H. Caspers, H.E. Rast, R.A. Buchanan, Energy levels of Pr^{3+} in LaF_3, J. Chem. Phys. 43 (1965) 2124–2128, https://doi.org/10.1063/1.1697083.

[50] C.K. Jørgensen, B.R. Judd, Hypersensitive pseudoquadrupole transitions in lanthanides, Mol. Phys. 8 (1964) 281–290, https://doi.org/10.1080/00268976400100321.

[51] B.R. Judd, Optical absorption intensities of rare-earth ions, Phys. Rev. 127 (1962) 750–761, https://doi.org/10.1103/PhysRev.127.750.

[52] D.E. Henrie, R.L. Fellows, G.R. Choppin, Hypersensitivity in the electronic transitions of lanthanide and actinide complexes, Coord. Chem. Rev. 18 (1976) 199–224, https://doi.org/10.1016/S0010-8545(00)82044-5.

[53] B.R. Judd, Ionic transitions hypersensitive to environment, J. Chem. Phys. 70 (1979) 4830–4833, https://doi.org/10.1063/1.437372.

[54] C.K. Jørgensen, R. Reisfeld, Judd-Ofelt parameters and chemical bonding, J. Less-Common Met. 93 (1983) 107–112, https://doi.org/10.1016/0022-5088(83)90454-X.

[55] M.G. Brik, A.M. Srivastava, Luminescent Materials, De Gruyter, 2023.

[56] T. Pier, T. Jüstel, Application of Eu(III) activated tungstates in solid state lighting, Opt. Mater. X 22 (2024) 100299, https://doi.org/10.1016/j.omx.2024.100299.

[57] J.-N. Keil, C. Paulsen, F. Rosner, R. Pöttgen, T. Jüstel, Crystallographic and photoluminescence studies on the solid solution $Li_3Ba_2La_{3-x}Pr_x(WO_4)_8$ (x = 0–3), J. Lumin. 252 (2022) 119415, https://doi.org/10.1016/j.jlumin.2022.119415.

[58] C.D.S. Brites, K. Fiaczyk, J.F.C.B. Ramalho, M. Sójka, L.D. Carlos, E. Zych, Widening the temperature range of luminescent thermometers through the intra- and interconfigurational transitions of Pr^{3+}, Adv. Opt. Mater. 6 (2018) 1701318 https://doi.org/10.1002/adom.201701318.

[59] K. Binnemans, Interpretation of europium(III) spectra, Coord. Chem. Rev. 295 (2015) 1–45, https://doi.org/10.1016/j.ccr.2015.02.015.

[60] K. Binnemans, C. Görller-Walrand, Application of the Eu^{3+} ion for site symmetry determination, J. Rare Earths 3 (1996) 173–180.